Theor. Comput. Fluid Dyn.
https://doi.org/10.1007/s00162-024-00729-7

ORIGINAL ARTICLE

Jason Appelbaum · Markus Kloker · Christoph Wenzel

A systematic DNS approach to isolate wall-curvature effects in spatially developing boundary layers

Received: 10 September 2024 / Accepted: 15 November 2024

Abstract A methodology to numerically assess wall-curvature effects in boundary layers is introduced. Wall curvature, which directly induces streamline curvature, is associated with several changes in boundary-layer flow. By necessity, a local radial pressure gradient emerges to balance mean flow turning. Moreover, a streamwise (wall-tangential) pressure gradient can appear for configurations with non-constant wall curvature or a particular freestream condition; zero pressure gradient is a special case. In laminar concave flow, the Görtler instability and the associated Taylor-Görtler vortices destabilize the flow and promote laminar-turbulent transition, whereas in the fully turbulent regime, unsteady coherent structures formed by the centrifugal instability mechanism dramatically redistribute turbulent shear stress. One difficulty of assessing centrifugal effects on boundary layers is that they often appear simultaneously with other phenomena, such as a streamwise pressure gradient, making their individual evaluation often ambiguous. For numerical studies of transitional and turbulent boundary layers, it is therefore beneficial to understand the interactive nature of such coupled effects for generic configurations. A methodology to do so is presented, and is verified using the case of a subsonic, compressible turbulent boundary layer. Four direct numerical simulations have been computed, forming a 2×2 matrix of turbulent boundary-layer states; namely with and without concave wall curvature, each having a zero and a non-zero streamwise-pressure-gradient realization. The setup and accompanying procedures to determine appropriate boundary conditions are discussed, and the methodology is evaluated through analysis of the mean flow fields. Differences in mean flow properties such as wall shear stress and boundary-layer thickness due to either streamwise pressure gradient or wall curvature are shown to be remarkably independent of one another.

Keywords Direct numerical simulation · Boundary layers · Wall curvature · Streamline curvature · Pressure gradient · Methodology

1 Introduction

The properties of wall shear layers are greatly affected by the presence of streamline curvature. Surface (wall) curvature, and thus streamline curvature in the adjacent fluid, is associated with the appearance of pressure gradients which balance the centrifugal acceleration of a fluid particle during transit through the flow field. For an inviscid, axisymmetric flow, the radial (r) momentum transport equation reduces to the transverse

J. Appelbaum (✉) · M. Kloker · C. Wenzel (✉)
Institute of Aerodynamics and Gas Dynamics (IAG), University of Stuttgart, Wankelstraße 3, 70563 Stuttgart, Germany
E-mail: appelbaum@iag.uni-stuttgart.de

C. Wenzel
E-mail: wenzel@iag.uni-stuttgart.de

M. Kloker
E-mail: kloker@iag.uni-stuttgart.de

Published online: 09 December 2024

pressure (p) equation $\partial p/\partial r = (1/r)\rho u_\theta^2$, where the right side of the equation is the centrifugal momentum term in which u_θ is the tangential velocity and ρ is the mass density. In the scope of laminar shear layers, the primary consideration regarding centrifugal effects is how the curvature of the flow affects stability and thus transitional properties. Early analytical considerations were made by Rayleigh [48], who showed that inviscid steady circular (axisymmetric) flow with radially decreasing angular momentum (i.e. $\partial(ru_\theta)^2/\partial r < 0$) is unstable with respect to an asymmetric disturbance. Experiments by Taylor [60] dealt with the stability of viscous laminar flow between concentric rotating cylinders, where it was demonstrated that by rotating the inner cylinder, instability would occur for a given envelope of Reynolds number Re and radius ratio, and the instability mode took the form of circumferentially aligned vortices. Clauser & Clauser [9] confirmed through experiment that laminar-turbulent transition in a curved channel occurred at an earlier point for the shear layer on the concave wall than on the convex wall. Perhaps the most well-known contribution regarding laminar stability and transition of centrifugal flows came from Görtler [19–21] who, based on viscous laminar stability analysis, predicted a mode and mechanism of instability for viscous concave wall flows, now referred to as 'Taylor-Görtler vortices' or simply 'Görtler vortices'. Such are rows of parallel vortices whose axes are aligned with the flow, occurring in counter-rotating pairs. As discussed in [4], both steady and unsteady vortices are amplified, the former dominating in transitional flows with very low background turbulence. The generalized inviscid, incompressible stability criteria for shear layers were summarized by Floryan [13], namely $\partial(u_\xi^2)/\partial\eta<0$ for concave walls and $\partial(u_\xi^2)/\partial\eta>0$ for convex walls, where η is the wall-normal coordinate. Thus, for monotonic velocity profiles, wall shear layers tend to be stabilized by convex wall curvature, whereas concave walls tend to destabilize. Thorough reviews of early work in the areas of streamline curvature and complex turbulent flows have been compiled by Bradshaw [5,6].

In the scope of turbulent shear layers, the focus tends to be on the manner in which the wall geometry affects the 'structure of turbulence', typically referring to the wall-normal distribution of Reynolds stresses $\overline{\rho u_i' u_j'}$ and terms of the Reynolds-stress transport budget, as well as their influence on the mean flow. The observations regarding the behavior of turbulent shear layers on concave/convex walls are a logical extension of the trends for the laminar case: turbulent energy production is amplified within concave-wall turbulent shear layers and inhibited along convex walls. Such has been observed and studied in detail in numerous experiments, e.g. [3,11,12,17,23,41,53–55,63]. In concave turbulent shear layers, large-scale coherent structures form by the same centrifugal instability as Taylor-Görtler vortices in the laminar case [3], however they are unsteady and irregular in span compared to their laminar counterparts as well as having very different properties, such as a lack of a well-defined core of vorticity, limited lifespan and shortened streamwise length [24]. In any case, the large coherent structures that form as a result of concave curvature introduce significant three-dimensionality into the turbulent shear layer, acting as a distinct mechanism for the redistribution of turbulent stress and making the concave turbulent shear layer fundamentally different from the convex turbulent shear layer. In the concave configuration, the centrifugal mechanism drives high-momentum fluid towards the wall, overwhelming the local radial pressure gradient, while low-momentum fluid is displaced and driven away from the wall to mix with the higher speed flow of the outer shear layer. The process modulates the near-wall cycle and accelerates turbulent transport, especially in the wall-normal direction. Turbulent shear layers on curved walls belong to a class of complex turbulent flows, defined as shear layers with complicating influences such as distortion by an extra rate of mean strain (beyond the classical cross-flow $\partial\bar{u}/\partial y$) or interaction with another turbulence field [6]. The effects of the centrifugal mechanism as well as the presence of the extra strain rate make the concave curvature case a critical and challenging turbulent flow.

Given the diverse applications in which curved turbulent shear layers are present, there is a clear need to be able to assess, understand and predict such turbulent flows. Early predictions of turbulent shear layers on curved walls were made by Prandtl ([45] found in [61], also [46]). His technique was based on methods originally developed for meteorology, given the analogy between the buoyancy-driven instability and the centrifugal instability. In short, it was reasoned that the classical mixing length could be multiplied by a function of dimensionless buoyancy or dimensionless curvature, which Prandtl originally derived for the centrifugal case through dimensional analysis. However, the originally derived function greatly underestimated the effects of turbulence in centrifugal flows. As a result, several empirical formulas were subsequently proposed to bridge this gap. Modern computational resources and turbulence-modelling techniques have improved the general ability to predict generic turbulent flows, though there are still notable shortcomings. One conclusion from the 1980/1981 conference on computation of complex turbulent flows held at Stanford University [28–30] was essentially that the techniques of the day were still unfit for curved-wall flows. Several modifications to two-equation models have been proposed, e.g. the modified $k-\epsilon$ model proposed by Launder, Priddin & Sharma

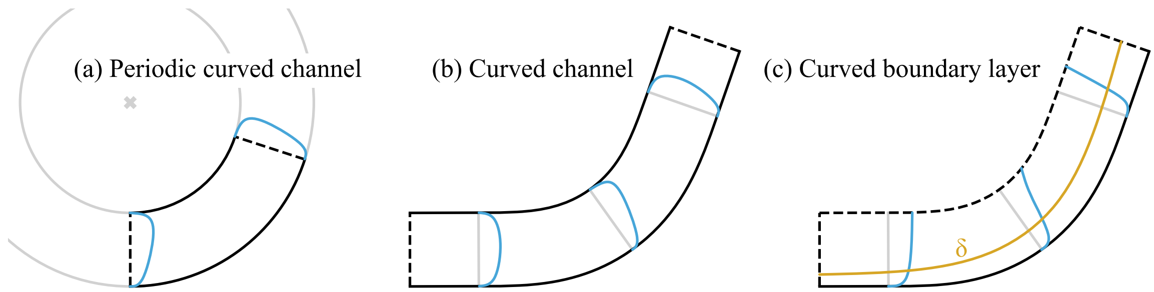

Fig. 1 Comparison of curved shear-layer cases. Blue lines indicate representative mean velocity profiles

[32], in which the transport equation for the dissipation rate ϵ is modified to be a function of wall curvature. Further evaluation of $k-\epsilon$ model adaptations for curved shear layers can be found in [49]. The most successful economical modelling techniques to date, excluding large-eddy simulation (LES), use a Reynolds-stress model (RSM) or algebraic RSM (aRSM) in which a separate model transport equation is solved for each component of the Reynolds-stress tensor, being either a partial differential equation (PDE) or an algebraic equation. Examples include the RSMs of Launder, Reece & Rodi [33] or Hanjalić & Launder [22] as well as the aRSM of Gibson [16]. Yang & Tucker [68] have tested the performance of a range of turbulence models, including an RSM, for the case of a curved channel, finding that essentially none of the models produced acceptable results. To summarize, it is unsurprising that turbulent flows over (concave) curved walls are still relatively difficult to predict, as they exhibit a significant reorganization of the transport and interaction of turbulent stresses, for example by large-scale coherent turbulent structures that come about due to the centrifugal mechanism.

1.1 State of the art from a DNS perspective

Among direct numerical simulation (DNS) studies of streamline curvature, at least three distinct cases can be distinguished which differ fundamentally in certain respects and have been researched with varying degrees of thoroughness: (1) the periodic curved channel, (2) the curved channel and (3) the curved boundary layer. Laminar-instability studies often adopt a simplified version of (3) with no streamwise pressure gradient, as in [56]. The case taxonomy is by no means exhaustive, for example impinging/wall-adjacent jets, rotating channels, curved pipes, rotating annuli, flow over bumps etc. are not addressed. Each of the three chosen cases is briefly introduced in the following sections.

1.1.1 Periodic curved channel

The periodic curved channel is an axisymmetric, fully developed channel as schematically illustrated in Fig. 1a. This case has the advantage of very well-defined boundary conditions, namely periodicity in the streamwise (circumferential, θ) and spanwise (z) directions and no-slip conditions at the radial boundaries. Furthermore, the configuration reaches an equilibrium state in which the circumferential dimension becomes statistically homogeneous. Early physical experiments by Wattendorf [63] and Eskinazi & Yeh [12] investigated the modification of the structure of turbulence by curvature in which a fully developed straight channel led into a circular section, where the flow eventually attained an equilibrium structure. Moser & Moin [40] performed a DNS of an incompressible curved periodic channel with relatively moderate curvature of $\delta/r_c = 1/79$, where δ in this case is the channel half-height and r_c is the radius of curvature at the channel centerline. Recently, Brethouwer [8] also thoroughly examined centrifugal effects in incompressible periodic channel flow in a DNS study which can be thought of as a higher Re extension of [40]. Three curved channels of various curvature δ/r_c were run and compared to the spanwise-rotating channel dataset from [7]. As commented upon in [8], the periodic streamwise condition tends to yield an inflow with more coherent structures, thus producing strong and coherent large-scale longitudinal structures which are a primary mechanism for redistributing turbulent stress within the turbulent shear layer on the concave (outer) wall. Furthermore, as was observed by Nagata & Kasagi [42] and mentioned by Brethouwer [8], for sufficiently thin channels there is significant interaction between the convex and concave shear layers, which hinders the extension to curved turbulent boundary layers.

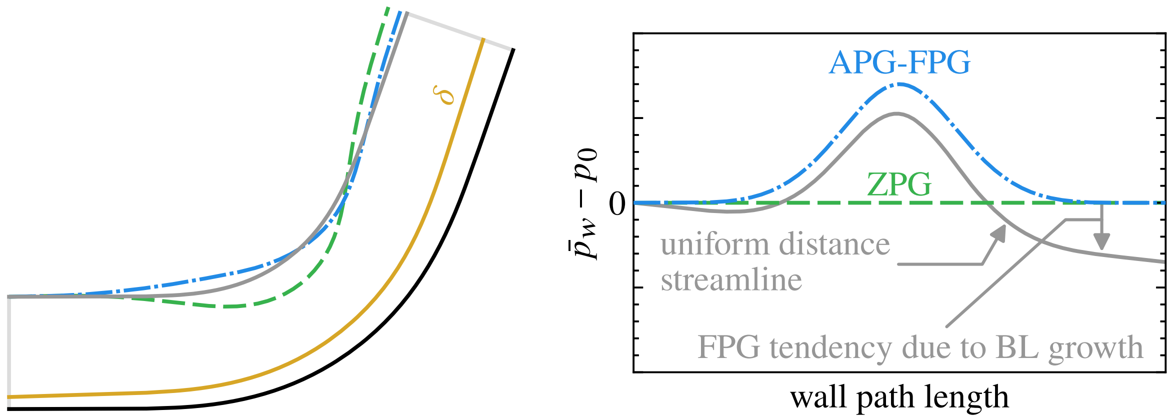

Fig. 2 Examples of freestream streamlines and their resulting mean wall pressure distributions

1.1.2 Curved channel

Many curved flows of engineering interest are not circular and/or not in equilibrium, rather the flow is subjected to a (potentially sudden) change in direction which brings about a transient response in the statistics of the flow. Moreover, the assessment of the equilibrium structure of turbulence in the fully developed periodic channel case cannot necessarily be assumed to extend to non-axisymmetric or non-equilibrium situations in which the shear layer exhibits a complex transient response, such as an ‘overshoot’ in statistical quantities as discussed in [53]. Thus, the setup depicted in Fig. 1*b* presents an extension of the periodic case in which an arbitrary channel geometry curvature is chosen, often having a nearly straight inflow section followed by a curved section. Monson et al. [38,39] examined a curved channel flow with a 180° bend, comparing experimental data obtained from multiple measurement methods to Reynolds-averaged Navier–Stokes (RANS) simulations. As validation for the rotation correction to the Spalart-Almaras turbulence model [57], Shur et al. [52] simulated both the 180° channel of [39] and the 90° channel of [27]. Yang & Tucker [68] evaluated the performance of various turbulence models for a turbulent channel with a 60° circular section by comparing to DNS results. It was noted that effectively no turbulence model, even the RSM tested, produced satisfactory results; the hypothesis for the shortcoming being that the linear approximation for the rapid pressure-strain correlation is a poor approximation for non-equilibrium flows, such as those experiencing sudden changes in wall curvature, and thus was the primary source of model error. The generalized, non-periodic curved channel is therefore a worthwhile case in need of further consideration. However, the designation as a ‘channel’ indicates that the shear layer flow is fully developed, and thus not growing into the irrotational core region outside the shear layer adjacent to the wall. External curved-wall flows or internal curved-wall flows that are still spatially developing therefore fall under the category of the curved boundary layer.

1.1.3 Curved boundary layer

In the curved boundary-layer case, the shear layer, now referred to as a boundary layer (BL), develops in the streamwise direction and grows in thickness, except when a strong favorable pressure gradient is present. By contrast, channels feature a fully developed profile in the area of interest. Therefore, the curved BL can be realized in a not-yet-fully-developed internal flow configuration in which the potential-flow core of the internal flow serves as the freestream. Such has been the typical procedure for notable physical curved-BL experiments, such as those described in [3,17,23,37,41,44,47,50,51,53–55,59,67]. The numerical curved-BL case requires the definition of a freestream (top) domain boundary as well as an inflow condition. Rather than discuss various numerical implementation options for freestream boundary conditions, it is more productive to consider a mean streamline induced by the freestream boundary condition, which is not necessarily aligned with the actual numerical domain boundary. The combination of wall geometry and freestream streamline will determine the streamwise component of the pressure gradient along the wall, an essential feature of non-axisymmetric curved-wall geometries. Note that a single streamline determines the potential-flow field i.e. freestream condition.

Fig. 2 schematically illustrates examples of three possible freestream streamlines and the mean wall pressure ($\bar{p}_w$) patterns that they induce. For a streamline parallel to the wall, i.e. a uniform-distance streamline (—), one can expect an adverse pressure gradient (APG) at the onset of curvature followed by a favorable pressure gradient (FPG) as wall curvature once again decreases. Due to the increasing displacement of the developing BL, there is an FPG tendency superimposed on the APG-FPG pattern. A second possibility (—·—) compensates for the displacement (thickness) development such that the FPG tendency is removed; the APG-FPG pattern is still present in the strongly curved region, outside of which there is zero pressure gradient (ZPG). A third possibility (– –) is a converging–diverging streamline which accelerates/decelerates the potential flow to compensate for any streamwise pressure gradient at the wall, thus maintaining ZPG over the curved surface. The experiment of Jeans & Johnston [24] used a contoured test section to enforce ZPG along a concave wall to avoid potentially complicating influences of streamwise pressure gradient. Similar measures have been taken in convex turbulent-boundary-layer (TBL) experiments, for example [17,18]. In 1996, Lund & Moin [36] performed an LES of a concave TBL based on the experimental setup of [3], allowing for discussion regarding the large-scale structures mentioned in the experiment. A 2015 study by Arolla & Durbin [1] used LES to examine an incompressible TBL on a concave wall without pressure-gradient compensation, using a slip-wall top boundary at constant wall distance. Thus, the flow is subject to both APG at the onset of curvature and developing streamline-curvature effects in the curved region. At the onset of curvature, the friction coefficient $c_f = 2\tau_w/(\rho U_\infty^2)$, where U_∞ is the freestream streamwise velocity and τ_w is the wall shear stress, is immediately reduced due to deceleration by the APG, whereas the collective effects of concave curvature yield a subsequent rise in c_f through the curved section. A 2021 study by You et al. [69] examined the influence of freestream turbulence on the spatial development of a curved TBL on a 90° curved wall section, asserting that the presence of freestream turbulence significantly modifies the character of outer roll motions induced by wall curvature, additionally pointing out the profound influence of streamwise wall pressure gradient on TBL development. Recently, Pargal et al. [43] investigated convex streamline-curvature effects on the suction side of an airfoil, specifically in the APG region in the downstream portion of the chord, and have compared to a flat-plate simulation with a matched mean wall pressure and acceleration parameter $K = (\nu/U_\infty^2)(dU_\infty/dx)$ for incompressible flow, where ν is the kinematic viscosity. The flat simulation utilized a derived velocity boundary condition at the top boundary to achieve the match. For the relatively mild curvature investigated, effects solely due to convex curvature seem to be dominated by the APG, though some comparisons, such as in c_f, show expected trends associated with convex curvature. If DNS is to be used as a tool to study curved BLs, the role of streamwise wall pressure gradient needs to be simultaneously explored. Pressure gradients are understood to significantly affect the properties of flat-plate TBLs [15,65]. However, the exact relative influence that they have on curved-wall BLs has not been thoroughly studied. To this end, a numerical setup is needed which is capable of achieving an arbitrary streamwise pressure gradient along an arbitrary wall geometry.

1.2 Goals of this study

The majority of the numerical research to date has been focused on curved channels such as those illustrated in Fig. 1 panels (*a*) and (*b*). However, spatially evolving curved TBLs are highly relevant in many practical applications, such as the contours of vehicles, turbine/fan blades, intake/discharge flows, junction flows, etc., and thus require attention. As alluded to in §1.1.3, the challenge associated with the study of curved TBLs is the unbounded parameter space formed by the choice of wall curvature and wall streamwise-pressure-gradient functions, the latter being influenced by the chosen freestream condition. A streamwise pressure gradient is a standard feature in flows over walls of variable curvature. Since the effects of both streamwise pressure gradient and streamline curvature are simultaneously present for general curved-wall flows, it becomes difficult to make conclusive assessments about the effect of streamline curvature alone. Thus, an approach is desirable that allows the independent assessment of both effects. A primary goal of this paper is to present and verify an approach capable of separating the effects of wall curvature from streamwise pressure gradient for the complex case of a spatially evolving TBL over a concave curved wall. It should be made clear that the methodology would not only be applicable for the fully turbulent regime, as will be discussed in the implementation example presented in §3, but also to e.g. laminar-turbulent transition and the influence of streamwise pressure gradient on the characteristics of Taylor-Görtler vortices and their formation in practical laminar flows.

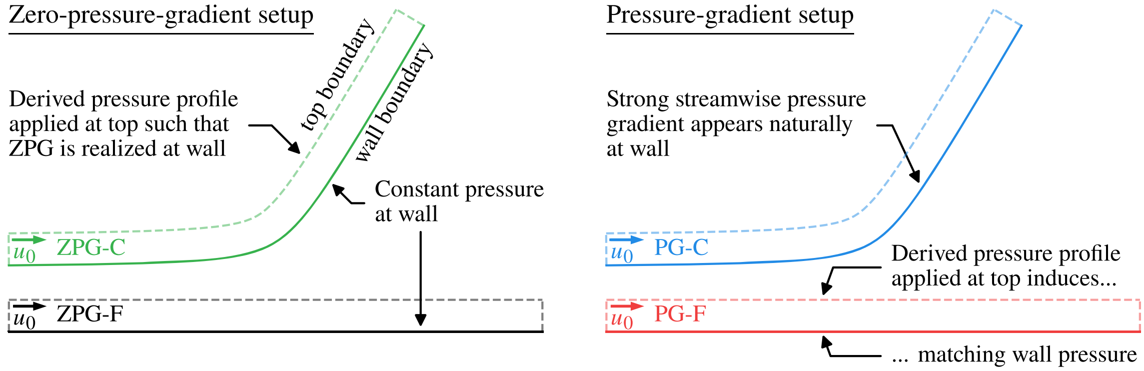

Fig. 3 Methodology illustration

Table 1 DNS case summary

Case ID	Description
ZPG-C	Curved-wall case with zero pressure gradient along wall
ZPG-F	Flat-wall case with zero pressure gradient along wall
PG-C	Curved-wall case with non-zero pressure gradient along wall
PG-F	Flat-wall case with mean wall pressure matched to PG-C

2 Methodology and numerical realization

2.1 Methodological approach

To isolate the influence of streamwise pressure gradient and wall curvature, the latter being inseparably associated with a wall-normal pressure gradient, a design of two pairs of DNS is proposed, each consisting of a curved-wall (C) case and a corresponding flat-wall (F) case. As visually indicated in Fig. 3 and summarized in Table 1, a nearly identical pressure profile in path length s along the wall is required within each pair.

2.1.1 Zero-pressure-gradient setup

The first pair of cases is comprised of a curved-wall ZPG case (ZPG-C) and a flat-wall ZPG case (ZPG-F), the former being achieved through the targeted modification of the domain top pressure profile such that nearly constant mean pressure is induced at the wall. Comparison of the two datasets reveals effects of streamline curvature in absence of mean streamwise pressure gradient at the wall.

2.1.2 Pressure-gradient setup

The second pair of cases (PG-C & PG-F) shares the same non-zero pressure gradient along the wall which has an APG-FPG form similar to that illustrated in Fig. 2. In the curved case PG-C, the rising and falling pressure profile along the wall is the natural consequence of the centrifugal effect on the flow induced by the increasing and decreasing wall curvature. At the top boundary, a normal velocity is allowed such that the FPG tendency is nullified before and after the curved region as discussed in § 1.1.3. For the flat case PG-F, the pressure distribution set at the domain top boundary is derived such that the resulting mean wall-pressure distribution matches that of the curved case PG-C. Comparison of PG-C & PG-F reveals effects of streamline curvature in the presence of streamwise pressure gradient at the wall.

2.1.3 Cross-comparison

Furthermore, the comparison between the curved ZPG case, ZPG-C, and the curved PG case, PG-C, allows for an assessment of the different effect of streamwise pressure gradient on the BL for equivalent (non-zero) wall curvature, whereas comparison of ZPG-F & PG-F enables an assessment in absence of wall curvature. The advantage of the study design is that it yields cross-comparable datasets while controlling for one or more factors. For example, the effect of mean flow turning (i.e. curved vs. flat wall) on the BL flow can be examined for equivalent streamwise pressure gradients (zero or non-zero). Similarly, for a given wall geometry, changes in the flow due to variation in streamwise pressure gradient can be studied. Such understanding is valuable for e.g. the development and refinement of reliable RANS codes.

2.2 Numerical realization

The success of the approach described above is highly dependent on the ability to achieve a matching wall pressure distribution between cases ZPG-C and ZPG-F and between PG-C and PG-F. However, creating a DNS setup that achieves a targeted mean pressure distribution at the wall is a non-trivial task for e.g. transitional and turbulent BLs, since the pressure at the wall is the result of the adjacent unsteady flow field and thus cannot be simply set. The mean wall pressure must therefore be indirectly induced by the domain top boundary condition. For generic, non-axisymmetric wall curvatures, the pressure field is two-dimensional and not easily derivable by e.g. the 1D transverse pressure equation. Therefore, the appropriate top condition and 2D steady flow field must be computed in order to derive the appropriate freestream condition.

2.2.1 2D steady solver

For the non-trivial task of deriving the necessary freestream domain boundary pressure distribution which will yield a targeted mean (in $[z, t]$) pressure profile at the lower wall boundary in the DNS (i.e. for cases ZPG-C and PG-F), some estimation or prediction method is required. Such could obviously take many forms. For the present study, a preprocessing tool was developed which solves the incompressible steady Navier–Stokes and continuity equations in 2D on a curvilinear grid. Sixth-order central explicit finite differences are used throughout the domain, and biased stencils of decreased order are used near the domain boundaries. The grid curvilinearity is handled through a metric transformation between the physical and logical grid coordinate spaces; the metric terms of the Jacobian are calculated numerically and the vector operators of the equations are formulated accordingly. For the solution of the 2D steady field, the lower boundary is treated as a slip wall with zero wall-normal velocity ($u_\eta = 0$) and zero wall-normal gradient in wall-tangential velocity ($\partial u_\xi / \partial \eta = 0$) as well as a set pressure ($p_w = f(s)$). No BL is included in the 2D solver solution. Viscous terms are kept active, however no significant sources of strain rate are present other than the velocity gradient induced by the deceleration due to wall curvature. The viscous terms are globally very weak in magnitude with respect to the convective terms. Therefore, the flow solution from the 2D solver can effectively be considered a solution of the 2D steady incompressible Euler equations (or potential-flow solution if no initial vorticity is assigned). The problem is solved as a global elliptical problem, i.e. no timestepping is involved and the temporal derivative terms $\partial/\partial t()$ are identically null. The non-linear convective terms are pseudo-linearized using the velocity field of the previous iteration. The discretized linear problem is solved using the PETSc framework and SuperLU_DIST for lower-upper factorization. Such is possible given the relatively small 2D problem size of $\mathcal{O}(10^6)$ points. Roughly 10 iterations of the pseudo-linearized system are needed to converge the non-linear convective terms to machine tolerance.

The main difficulty during the 2D steady field solution process is the relative ill-posedness of the boundary conditions, which is understandable given that its own purpose is to approximate necessary freestream conditions for the DNS. The wall boundary can either have a set pressure applied and slip-wall conditions ($u_\eta = 0$, $\partial u_\xi / \partial \eta = 0$) or, equivalently, a potential wall-tangential velocity $u_{\xi,pw} = \sqrt{(2/\rho)(p_{t,0} - p_w)}$ can be set while leaving the pressure to self-adjust based on a zero-gradient condition, where p_w is the targeted wall-pressure function and $p_{t,0}$ is the inlet total pressure. However, no 'strong' condition is immediately available for the upper boundary, thus a zero-gradient condition (normal to the boundary interface) is set for u_ξ, u_η and p.

2.2.2 DNS procedure

Using the 2D steady solver described in §2.2.1, an initial flow solution is generated where the target wall pressure profile is prescribed as a boundary condition. Subsequently, the 2D $[u, v, p]$ fields are converged and the resulting 1D pressure along the top boundary is extracted to be applied as a quiescent Dirichlet boundary condition in an under-resolving version of the 3D DNS, which for convenience will be oxymoronically referred to as a 'coarse DNS'. The coarse DNS runs roughly 50× faster compared to the DNS on the same computational hardware for a given simulation time duration, and the 2D steady solution requires effectively negligible resources. As the 2D inviscid flow solution can only estimate the correct freestream condition, the first coarse DNS result usually shows a pressure distribution at the wall with about 3% error compared to the targeted distribution. Thus, based on the $[z, t]$ mean of the coarse DNS, the input wall pressure boundary condition for the next iteration of the 2D solver is adjusted based on the difference between the target pressure profile and the mean result of the coarse DNS. For example, the wall pressure set in the 2D solver is reduced where the mean wall pressure from the averaged field of the coarse DNS is too high (compared to a target p_w), and vice versa. The procedure can be thought of as a predictor-corrector method for non-linear root-finding. Obviously, the incompressible inviscid 2D predictor solution does not take into account compressibility, viscosity, BL displacement, three-dimensionality of the flow or the effect of turbulence on the mean flow; such is the task of the 3D corrector. The 2D predictor only needs to provide a robust solution in the face of a relatively ill-posed problem and point in the right direction (in root space) given an accumulated $\Delta p = p_{w,\text{target}} - \bar{p}_{w,\text{corrector}}$. The process has been found to be quickly convergent, and can be repeated until the resulting pressure distribution at the wall reaches a desired relative difference in mean wall pressure for a given pair of cases. Ultimately, the final DNS is carried out on a fully resolving DNS grid. Maximally three iterations have been necessary for most cases to reach acceptably low relative differences, representing about 6% of the computational cost of the final DNS for the procurement of boundary conditions. The use of the relatively simple and transparent 2D Euler solution as a predictor has proven effective and consistent for the present cases, and would be expected to work similarly well for any unseparated flow at arbitrary Re and subsonic Mach number, as the 2D predictor only 'sees' a Δp from the 3D coarse DNS corrector which accounts for compressibility, among other real flow effects. The procedure has not been attempted for highly compressible cases, i.e. the supersonic regime, however existing nozzle-design codes might prove useful as a replacement predictor method.

3 Realization for the case of a turbulent boundary layer

As introduced in §1, the spatially evolving TBL over a concave wall in particular is a topic of great interest and is therefore selected as a candidate to test both the approach and the numerical realization proposed in the previous section. To enable a standardized description of the flow, the wall contour has been defined as a hyperbola. The BL flow is treated as compressible with an inflow freestream Mach number of $M_0 = 0.5$. The geometric definition will first be introduced in §3.1, followed by a description of the DNS setup, in §3.2. Subsequently, a brief summary of the key results is given in §3.3 to enable the reader to assess the success of the study design.

3.1 Geometric definition and nomenclature

For the two curved setups, the geometric definition of the wall is prescribed by a hyperbola

$$\frac{x^2}{a^2} - \frac{y^2}{b^2} = 1, \tag{1}$$

providing a continuous, smooth transition between the curved area of interest and the nearly flat post-inlet and pre-outlet sections as illustrated in Fig. 4. The hyperbola is rotated such that one asymptote line is colinear with the global x axis. In Eq. (1), a and b are free parameters that are analytically re-parameterized in terms of a minimum radius of curvature $R_{\min}$ and opening angle φ_{open} (angle between asymptotes) of the hyperbola. The ramp angle is defined as $\varphi_{\text{ramp}} = \pi - \varphi_{\text{open}}$.

As shown in Fig. 4, a global Cartesian $[x, y, z]$ system is defined, where $[u, v, w]$ are the velocity vector components in the corresponding directions. To indicate a local wall-aligned Cartesian system, $[\xi, \eta, z]$ are used, where ξ indicates the local wall-tangential direction and η indicates the local wall-normal direction. In the local system, the origin $[\xi, \eta] = [0, 0]$ is located at the wall boundary. The variable s indicates the 1D integrated path length along the wall, with $s = 0$ chosen to be at the hyperbola vertex, where $R_{\min}$ also occurs. The letter R indicates the local radius of curvature of the wall, which for the non-circular case is not constant, i.e. R is a function of the parametric wall position s. The radial coordinate of the local cylindrical system is indicated by r. The wall-normal position vector η and the radial position vector have the relationship $\eta = R - r$ if the origin of the local cylindrical system is placed at $\eta = R$. For the flat cases (ZPG-F & PG-F), ξ and η simply correspond to a translated local $[x, y]$ coordinate system.

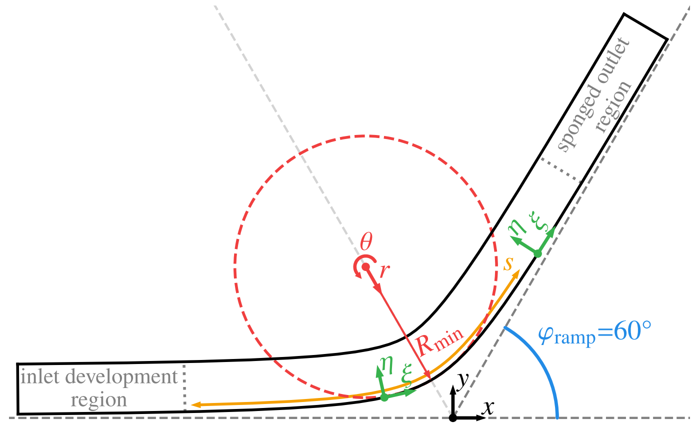

Fig. 4 Coordinate systems and curved-domain illustration

The BL thickness of the inlet velocity profile δ_0 is used as a constant global characteristic length scale for non-dimensionalization of the domain coordinates and is equal for all four cases. Quantities with a 'zero' subscript $\square_0$ refer to the inlet freestream definition and are constant global values being equal for all four cases. The freestream flow is accelerated and decelerated by the centrifugal effects of curvature and pressure gradient within the domain. The wall-normal location of the effective interface between BL and the freestream, the BL edge, is determined where the z-component of the mean vorticity $\bar{\omega}_z \approx 0$, with a small numerical-noise tolerance ϵ

$$\delta_e(\xi, \eta) = \eta(\xi, \eta(\left|\bar{\omega}_z^+\right| < \epsilon)). \tag{2}$$

Quantities at the BL edge are indicated by the subscript 'e' ($\square_e$) and represent the local freestream state. The 99% hydrodynamic BL thickness is defined as

$$\delta_{99} = \eta(\breve{u}{=}0.99{\cdot}\breve{u}_e), \tag{3}$$

where the pseudovelocity $\breve{u}_e$ is a wall-normal integration of $-\bar{\omega}_z$ [58]. Time-averaged quantities are indicated by an overline ($\bar{\square}$), and mean-removed quantities by superscript 'prime' ($\square'$). Normalization using inner characteristic scales is denoted by superscript 'plus' ($\square^+$). The inner velocity scale is the local friction velocity $u_\tau = \sqrt{\tau_w/\bar{\rho}_w}$, where subscript '$w$' denotes the wall location $\eta = 0$, $\tau_w = \bar{\mu}_w(\partial\bar{u}_\xi/\partial\eta)_w$ is the mean streamwise wall shear stress, ρ is the volumetric mass density and μ is the dynamic viscosity.

3.2 DNS setup

3.2.1 DNS Code NS3D

All DNS in the present study have been performed with the code 'NS3D' developed at the Institute of Aerodynamics and Gas Dynamics (IAG) at the University of Stuttgart. NS3D solves the 3D dimensionless compressible Navier–Stokes equations together with the continuity and energy equations in conservative formulation on a block-structured curvilinear grid. Details of the code and its numerical procedure can be found in [2,25,26,34,35,64]. Spatial gradient operators of the fluid transport equations are discretized using eighth-order explicit finite differences. Convective terms are discretized with temporally alternating upwind and downwind-biased stencils as described in [31]. The classical fourth-order Runge–Kutta scheme is used for temporal integration. A spatial tenth-order implicit filter is used to attenuate numerical noise associated with discretization error as specified in [10,62].

3.2.2 Numerical setup

According to the methodology introduced in §2.1, a total of four DNS are computed: two curved and two flat cases which are described in Table 1. For the curved setups ZPG-C and PG-C, a ramp angle φ_{ramp} =

$\pi - \varphi_{\text{open}} = \pi/3 = 60°$ and a minimal radius of curvature of $R_{\min}/\delta_0 = 78.402$ are used, corresponding to $a = 26.134$ and $b = 45.265$ in Eq. 1. The choice of $R_{\min}$ yields a curvature ratio $R_{\text{ref}}/R_{\min} = 30$, where R_{ref} is the radius of curvature at a reference location $s/\delta_0 \pm 125$ and $R_{\min}$ is $R(s = 0)$. For all cases, the freestream Mach number of the mean inlet profile is $M_0 = 0.5$. The specific gas constant R, the ratio of specific heats $\gamma = c_p/c_v = 1.4$ and the Prandtl number $Pr = 0.71$ are constant.

All four DNS use a single curvilinear structured grid block comprised of [7424, 344, 1328] points in $[x, y, z]$, for a total of 3.39×10^9 points. Presently, $[x, y]$ is used interchangeably with $[\xi, \eta]$, as the curved domains are dimensionally consistent but geometrically curved versions of the flat domains. The domain dimensions are $[L_x, L_y, L_z] = [500, 30, 40]$ in characteristic length units δ_0. The domain width L_z and height L_y are determined such that $L_z/\delta_{99,\max} > 4$ and $L_y/\delta_{99,\max} > 3$, where $\delta_{99,\max}$ is the BL thickness at $s = +150$ for the more restrictive curved cases as quantified in Fig. 7(b). At the wall, the grid is uniformly spaced in the wall-tangential direction in the domain area of interest such that $\Delta x^+_{\max} \lesssim 7$. The 2D $[x, y]$ grid is constructed by projecting a fixed 1D wall-normal point coordinate distribution in the local wall-normal direction from each wall point. The 3D grid is then a projection of the 2D grid in z. In the wall-normal direction, the grid is stretched starting from a wall spacing of $\Delta y^+_{w,\max} \lesssim 0.8$. In the spanwise direction, a uniform grid is used such that $\Delta z^+_{\max} \lesssim 4$. After an initial transient phase of $\Delta t/(L_x/u_0) \gtrsim 2$, the measurement phase is started in which statistical averaging (in $[z, t]$) and output of unsteady data are performed. The duration of the measurement phase is $\Delta t/(\delta_{99}/u_\tau)_{\max} \gtrsim 7$.

3.2.3 Boundary conditions

At the domain inlet boundary, a digital-filtering procedure is used to generate a turbulent inflow [14,64,66]. The mean inlet profile has been determined through an auxiliary simulation and has a momentum-thickness Reynolds number of $Re_\theta \approx 230$, where $Re_\theta = \theta u_{\xi e}\rho_e/\mu_e$ and θ is the momentum thickness $\int_0^{\delta_e} (\bar{\rho}\bar{u}_\xi)/(\rho_e u_{\xi e})\cdot(1 - (\bar{u}_\xi/u_{\xi e}))d\eta$. An induction length of $\sim 100\delta_0$ is provided downstream of the digital-filtering inlet (and upstream of the area of interest) for the development of the BL and rebalancing of the artificially produced turbulent field. Upon entrance to the domain area of interest $s = -150$, all four DNS have nearly identical mean velocity profiles with $Re_\theta = 989.2 \pm 4.7$. At the outlet boundary, the time derivative of the vector of conservative flow variables $Q = [\rho, \rho u, \rho v, \rho w, E]$ is spatially extrapolated such that $\partial Q/\partial t|_i = \partial Q/\partial t|_{i-1}$, where i indicates the grid x index. Streamwise grid stretching as well as a numerical sponge are applied upstream of the outlet boundary to attenuate the turbulent field. The domain lower boundary is an adiabatic no-slip wall with $(\partial T/\partial \eta)_w = 0$ and $\mathbf{u} = \mathbf{0}$ as well as $(\partial p/\partial \eta)_w = 0$. A one-sided fifth-order finite-difference stencil for the derivative at the wall, set to zero, is used to compute the wall values of p and T. At the domain upper boundary, zero-gradient conditions are set for all velocity components and T, whereas p is set explicitly from the profile solved during the process described in §2. A numerical sponge is used in the region immediately adjacent to the top boundary to damp and inhibit the reflection of acoustic waves. Both spanwise boundaries are periodic.

3.3 Results

3.3.1 Mean pressure distribution

Figure 5 depicts the mean pressure distributions of the two ZPG cases in panel (a) and the two PG cases in panel (b). The pressure distributions at the wall and at the freestream (top) boundary are plotted for each of the four cases. The top boundary pressure profiles were obtained from the 2D solver solution and set as a boundary condition in the DNS. Note that the following results were obtained with two additional coarse DNS iterations for the ZPG setup and without an additional iteration for the PG setup.

For the ZPG setup in panel (a), both the flat case (ZPG-F) and the curved case (ZPG-C) are characterized by an almost perfect ZPG condition at the wall. Note that the ZPG-C wall line (—) vanishes behind the ZPG-F wall line (–··–). The pressure distribution at the top boundary of ZPG-C (solution of the 2D solver, – –) deviates drastically from a constant distribution, by necessity. Physically, this simply reflects the fact that the top boundary condition must force the streamlines towards the wall to create a nozzle flow that accelerates the fluid to compensate for the otherwise increased wall pressure associated with the centrifugal effect of flow turning.

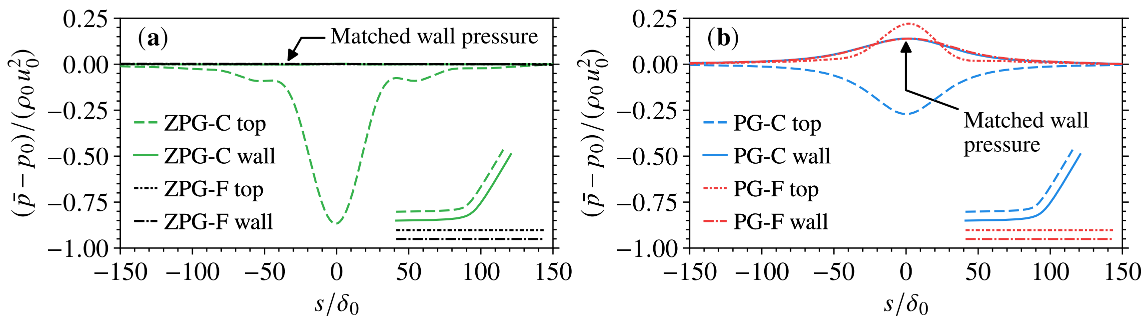

Fig. 5 Wall and top boundary mean pressure distributions for ZPG cases (**a**) and PG cases (**b**)

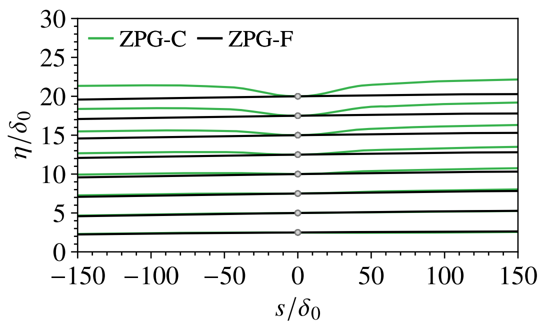

Fig. 6 Convective pathlines generated from mean flow. Gray circles indicate the initial positions for forward/backward integration

For visual illustration, Fig. 6 shows a set of pathlines generated using the $[z, t]$ mean of the DNS field; initial positions are chosen at several wall-normal locations for $s = 0$, as indicated by the gray dots. Near the wall, the lines are virtually identical, whereas with increasing wall distance one can see the effect of the local acceleration (thinning) followed by deceleration (thickening) of the flow, forced by the top-boundary pressure profile. The interested reader may compare to Fig. 5 of [24].

For the PG setup in Fig. 5(*b*), in contrast, the wall pressure increases continuously up to approximately the position $R_{\min}$ at $s = 0$, and decreases thereafter towards ZPG conditions. Essentially, the pressure distribution is the direct effect of the transverse pressure relation, which necessitates a negative wall-normal (positive radial) pressure gradient inversely proportional to the local curvature radius of the wall and thus the adjacent flow. The top pressure profile of PG-C (– –) was determined from the 2D Euler solver with slip-wall conditions at both the lower and top boundaries. By allowing flow normal to the top boundary in PG-C, the increasing displacement of the TBL does not lead to a global FPG tendency as illustrated in Fig. 2. Instead, a ZPG is approached outside of the strongly curved region. In the curved region around $s = 0$, an APG is present where wall curvature $(1/R)$ increases with s and an FPG is present where curvature decreases. The computed mean wall pressure from PG-C (—) was set as the target profile to be matched in PG-F (–·–). As seen in Fig. 5(*b*), the mean wall pressures agree very well. For PG-F, the top boundary pressure derived from the 2D solver (·····) shows a much more pronounced pressure peak compared to the targeted pressure peak at the wall. In PG-C, the non-zero centrifugal momentum term $\bar{\rho}\tilde{u}_\theta^2/r$ is balanced by $\partial\bar{p}/\partial r$, which by the convention of Fig. 4 is positive in magnitude. Consequently, $\partial\bar{p}/\partial\eta < 0$, hence pressure decreases with increasing wall distance. Accordingly, the top boundary pressures of ZPG-C (– –) and PG-C (– –) are lower than at the wall as seen in Fig. 5. In PG-F however, no such centrifugal term momentum source exists, therefore a higher and 'pointier' pressure distribution must exist at the top boundary (·····) to relax towards the wall and maintain equilibrium with the target pressure profile.

3.3.2 Streamwise evolution of mean-flow quantities

The previous section has verified that both the approach as well as its numerical realization are successful in delivering DNS that have virtually perfectly matching mean wall-pressure distributions for arbitrary geometries. The goal of the present section is to identify to what extent the effect of streamwise pressure gradient and wall curvature can be isolated in terms of the streamwise evolution of mean BL quantities such as τ_w and δ_{99}.

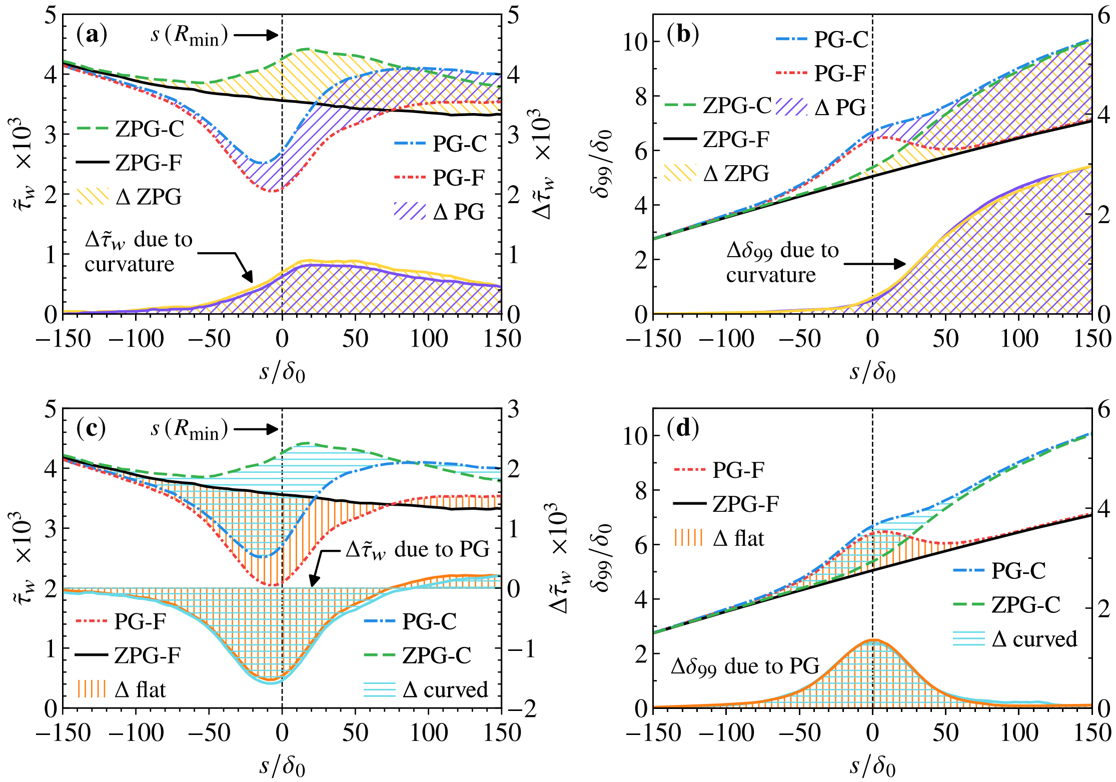

Fig. 7 Streamwise progression of normalized wall shear stress $\tilde{\tau}_w$ (**a**,**c**) and boundary-layer thickness δ_{99} (**b**,**d**)

To this end, the effects of wall curvature and streamwise pressure gradient on both variables are addressed in Fig. 7 by a cross-comparison of all four DNS cases. In Fig. 7, the progressions of normalized wall shear stress $\tilde{\tau}_w = 2\tau_w/(\rho_0 u_0^2)$ are plotted in panels (a) and (c); the effect due to wall curvature is highlighted in panel (a) and the effect of the streamwise pressure gradient is featured in panel (c). ZPG-C (– –) sees a significant increase in $\tilde{\tau}_w$ compared to ZPG-F (—) due to the extra strain rate associated with mean flow turning and the forcing of higher momentum flow towards the wall. Both PG-C (–·–) and PG-F (·····) initially experience a reduced $\tilde{\tau}_w$ due to the APG for $s \lesssim 0$, followed by an increase in the FPG region $s \gtrsim 0$. Both PG cases slightly overshoot their respective geometric counterparts in $\tilde{\tau}_w$ downstream.

To assess to what extent the $\tilde{\tau}_w$ increase due to wall curvature is comparable in the presence and absence of streamwise pressure gradient, $\Delta\tilde{\tau}_w$ is plotted in panel (a) for the difference between ZPG-C and ZPG-F in yellow (\\\\\\\\) and between PG-C and PG-F in purple (////). The operator Δ indicates a difference between two quantities. Overall, both $\Delta\tilde{\tau}_w$ distributions show largely similar trends with only small differences in the absolute values remaining, indicating that the $\tilde{\tau}_w$ increase caused by mean flow turning can be largely considered to be independent of streamwise pressure gradient at the wall. To further assess to what extent the $\tilde{\tau}_w$ variation due to streamwise pressure gradient is comparable in the presence and absence of concave wall curvature, $\Delta\tilde{\tau}_w$ is plotted in panel (c) for PG-C and ZPG-C in light blue (☰) and for PG-F and ZPG-F in orange (||||). Interestingly, the presence or absence of concave wall curvature does not greatly effect $\Delta\tilde{\tau}_w$ caused by streamwise pressure gradient, as indicated by the very comparable $\Delta\tilde{\tau}_w$ distributions, which again only slightly differ between the two case pairs.

The progressions of the hydrodynamic BL thickness δ_{99} given in panels (b) and (d) are evaluated following the same strategy as for $\tilde{\tau}_w$. The development of δ_{99} reveals that both concave wall curvature and APG produce an increase in δ_{99}, whereas FPG decreases δ_{99}. The growth of the TBL ($\Delta\delta_{99} > 0$) due to concave wall curvature is evaluated both in the presence (////) and absence (\\\\\\\\) of streamwise pressure gradient in panel (b). As for the $\Delta\tilde{\tau}_w$ distributions before, only very small differences are observable between the two $\Delta\delta_{99}$ distributions, indicating that the increase in δ_{99} due to mean flow turning can also be largely considered to be independent of streamwise pressure gradient. For concave wall flows, fluid with higher angular momentum than that which the local radial pressure gradient can sustain is first driven towards the wall before being deflected. The thickening process of the TBL due to wall curvature is in part a consequence of the complex mixing process that this effect accelerates, thus it extends over a considerable region, causing the main increase in $\Delta\delta_{99}$ to occur relatively far downstream of $s = 0$. By contrast, in panel (d) one sees that the thickening ($\Delta\delta_{99} > 0$) due to streamwise pressure gradient both in the presence () and absence () of surface curvature is more or less immediate, as it is associated with the local acceleration/deceleration of the BL, thus $\Delta\delta_{99}$ is approximately symmetrical with respect to $s = 0$. In line with all previous results, the variations in δ_{99} due to streamwise pressure gradient can also be considered to be largely comparable for cases both with and without wall curvature in panel (d).

This section demonstrates that for the τ_w and δ_{99} distributions (apart from minor deviations that may be largely due to an imperfectly calibrated pressure distribution), the effects of streamline curvature and streamwise pressure gradient can be separated quite well, at least for the variables considered. As Fig. 7 has illustrated, both curvature and streamwise pressure gradient induce dramatic effects on τ_w and δ_{99} in absolute terms, although differential comparison reveals remarkably independent trends. The degree of independence of the mean flow is a significant finding of the present work which has been made possible by the study's design.

3.3.3 Wall-normal profiles

In the previous section, the differences in BL thickness $\Delta\delta_{99}$ and normalized wall shear stress $\Delta\tilde{\tau}_w$ along the wall induced by surface curvature and streamwise pressure gradient have been shown to be nearly independent of the presence or absence of the other feature. Although this result was expected to some degree – in essence, it was the motivation for this DNS setup approach – the actual extent to which it works might be quite surprising. Thus, it must be explicitly emphasized at this point that the previous discussion dealt solely with BL quantities which, in a certain sense, evaluate only the integral response of a BL to changed flow conditions. For example, $\tilde{\tau}_w$ and δ_{99} incorporate the consequences of the physical processes within the BL at a given streamwise position. Thus, even if the effects of wall curvature and streamwise pressure gradient appear to be independent for e.g. $\tilde{\tau}_w$, this by no means necessarily also applies for the wall-normal BL profiles which encapsulate the structure of turbulence within the TBL. To visually demonstrate this statement, wall-normal profiles of the mean streamwise velocity $\bar{u}_\xi$ and turbulent shear variance $-\overline{u'_\xi u'_\eta}$ are shown in Fig. 8. The profiles are evaluated at $s = +20$, in the region downstream of $s = 0$ (see Figs. 9 and 10 for orientation) where the effects of streamline curvature and streamwise pressure gradient have had a chance to reorganize the TBL flow fields. Figure 8(a) shows the wall-normal profiles of the mean streamwise velocity $\bar{u}_\xi$ for all four cases. The profiles of PG-C () & PG-F () are still visibly decelerated from the APG region ($s \lesssim 0$) compared to their ZPG counterparts ZPG-C () & ZPG-F (), respectively. Due to the centrifugal instability and the extra mean strain rate, the mean velocity profiles of the curved ZPG-C () & PG-C () cases are fuller compared to ZPG-F () & PG-F () and, concurrently, the rate of strain at the wall is increased. For the curved cases, the tangential velocity outside the BL $\bar{u}_\xi$ becomes approximately equivalent to the potential velocity u_p (shaded lines) which is derived based on the local far-field circulation Γ, calculated as the average circulation beyond the BL edge $\Gamma = \left(\bar{u}_\xi r\right)_{>e}$. Using the potential-vortex analogy $\Gamma(r) = const. = u_p r$, the local potential tangential-velocity profile is $u_p(r) = \Gamma/r$ and the potential wall velocity $U_{pw} = \Gamma/R$ is simply an extrapolation to the wall ($r = R$). With the relation $\eta = R - r$, it follows $u_p = \Gamma/r = U_{pw}/(1 - \eta/R)$. Note that R is not defined as negative in magnitude in the present work as is occasionally the convention for concave walls. For the flat cases with $R = \infty$, the edge velocity u_e is used for U_{pw}. The wedge-shaped envelope formed by the potential profiles between matched streamwise pressure gradient case pairs, i.e. for ZPG-C & ZPG-F and PG-C & PG-F, illustrates the extra mean strain rate which the curved TBLs are subjected to during their development. Furthermore, the agreement in potential wall velocity U_{pw} supports the accuracy of the streamwise-pressure-gradient matching procedure, at least for the purposes of verifying the design of experiment. In Fig. 8(b), the velocity profiles normalized by u_p are shown. Such attempts to normalize for the local extra strain rate $\partial u_p/\partial\eta$ as well as the mean acceleration/deceleration associated with streamwise pressure gradient. However, even after normalization by u_p, the profiles are still very different in form and do not collapse based on either streamwise pressure gradient or wall curvature. Such is evidence for the complex and interactive effects of streamwise pressure gradient and wall curvature on the structure of the turbulent field.

Although the focus of the present work is on methodology and verification of the study design, and not a thorough investigation of turbulence statistics, profiles of two important turbulent quantities are shown in Fig. 8 panels (c) and (d). The inviscid centrifugal mechanism associated with concave curvature, which forces high-momentum fluid towards the wall and displaces low-momentum fluid, amplifies $-\overline{u'_\xi u'_\eta}$ as shown in

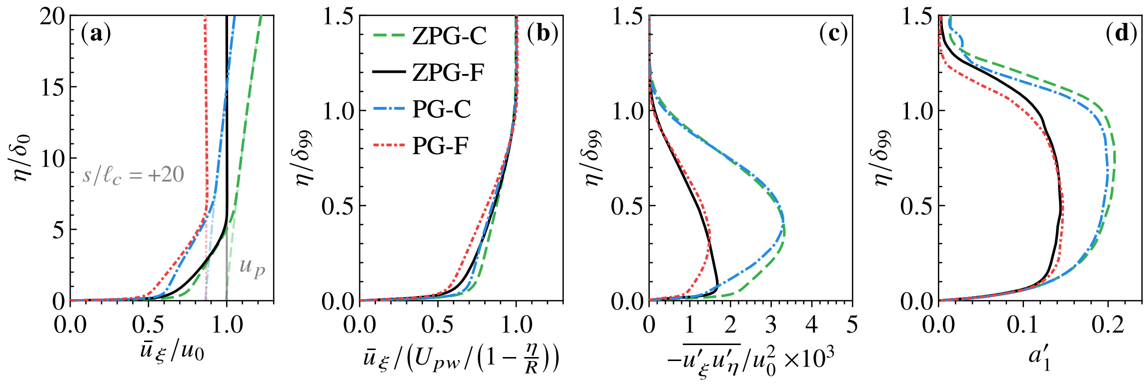

Fig. 8 Wall-normal profiles at $s/\delta_0 = +20$

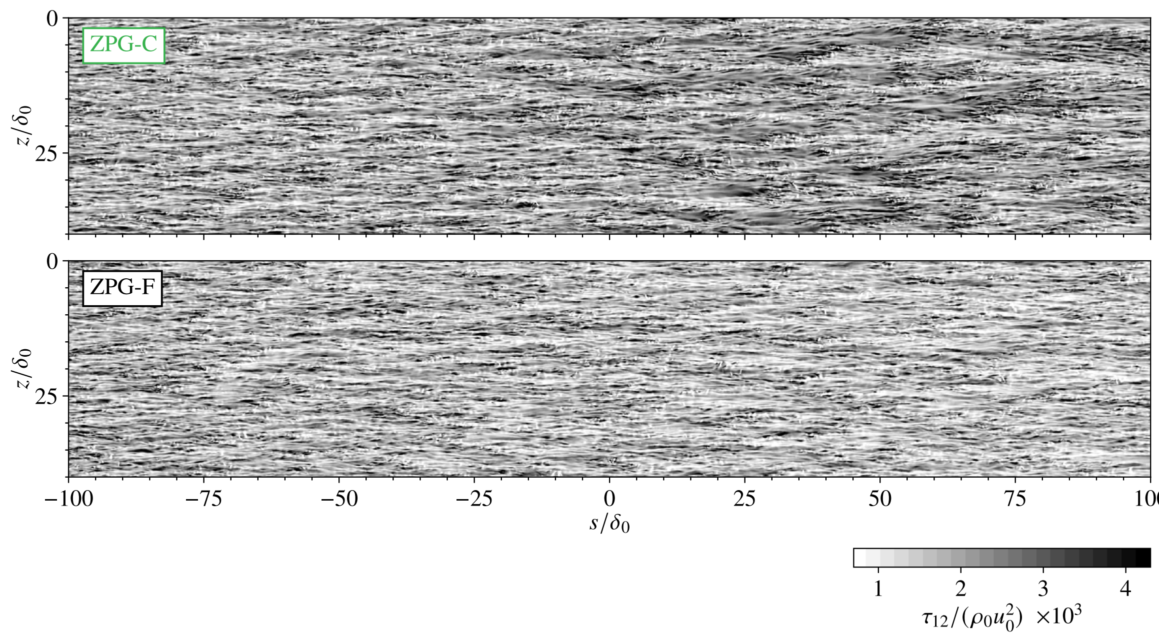

Fig. 9 Instantaneous wall shear stress

Fig. 8(c). For $\eta/\delta_{99} \gtrapprox 0.4$, the profiles of equivalent curvatures collapse remarkably well when using u_0 for non-dimensionalization, regardless of streamwise pressure gradient and the associated relative difference of >10% in $u_{\xi e}$ visible in panel (a). Closer to the wall, the streamwise pressure gradient appears to have a large influence. Figure 8(d) presents the two-component shear stress parameter

$$a'_1 = \frac{-\overline{u'_\xi u'_\eta}}{(3/2)(\overline{u'_\xi u'_\xi} + \overline{u'_\eta u'_\eta})},$$

which is simply the ratio of shear variance to in-plane turbulent kinetic energy. A decent collapse for equivalent curvatures is clear, indicating that, when normalized by the normal (isotropic) variances, the shear variance is relatively agnostic to the presence/absence of streamwise pressure gradient, although it clearly increases in prominence due to concave wall curvature.

3.3.4 Instantaneous flow field

For illustration purposes and to qualitatively support the discussion provided so far, it is valuable to inspect the instantaneous DNS flow field and visualize the structural changes in the turbulent flow due to wall curvature.

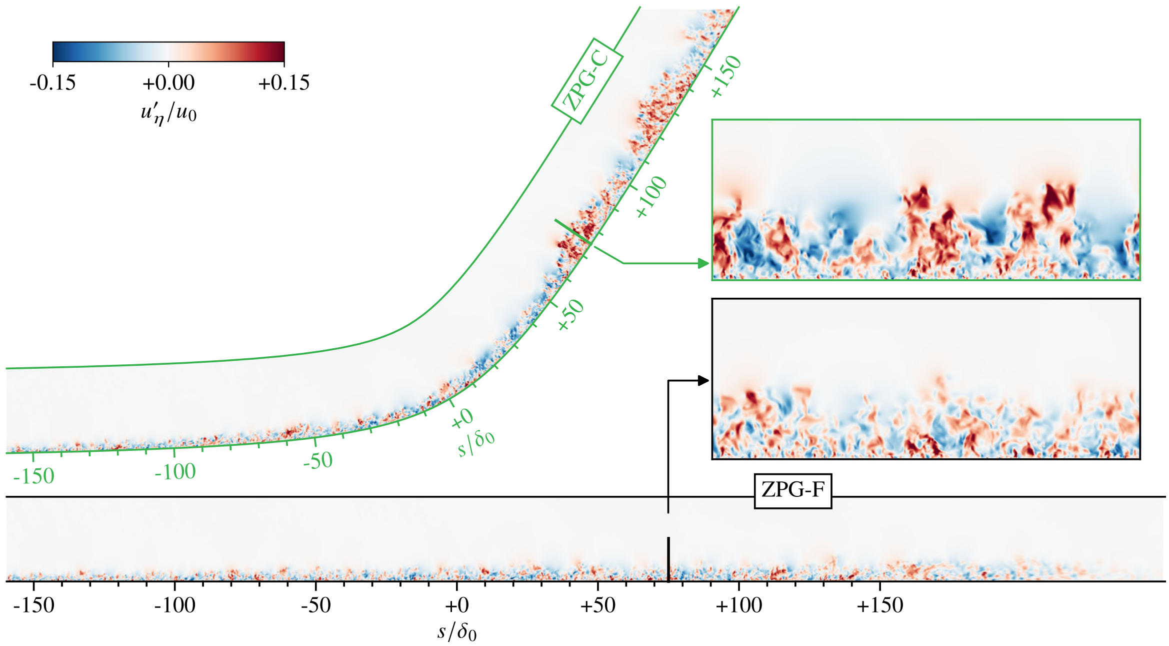

Fig. 10 Instantaneous wall-normal velocity fluctuation at $z/z_{\max} = 0.5$ and in a cross-cut at $s/\delta_0 = 75$

Figure 9 shows the instantaneous shear stress $\tau_{12} = \mu\left(\partial u_\xi/\partial\eta\right)$ at the wall ($\eta = 0$) for ZPG-C & ZPG-F. Compared to ZPG-F, ZPG-C clearly experiences much higher wall shear stress after the consequences of the centrifugal instability have had a chance to set in, as is also visible in the $\tilde{\tau}_w$ progression of Fig. 7. Furthermore, the pattern of τ_{12} is noticeably altered for $s \gtrsim 0$. Specifically, one can see large regions of enhanced wall stress due to sweeps of high-momentum fluid towards the wall. The relatively large coherent regions of higher shear stress appear to be superimposed upon the typical pattern of streaks associated with the lifecycle of the attached hairpin vortices.

Fig. 10 shows the instantaneous u'_η on z-normal and ξ-normal planes. The amplitude and large-scale organization of u'_η is clearly modified by the destabilizing tendency of the concave wall curvature. Not only are fluctuations stronger, but one can easily identify much larger coherent regions of fluctuation.

4 Conclusions

A methodology has been described which enables the exploration of wall-curvature effects on spatially evolving boundary layers, taking into account the presence of a streamwise pressure gradient. To this end, a study consisting of two pairs of DNS is devised, each consisting of a curved-wall (C) case and a corresponding flat-wall (F) case, forming a 2x2 run matrix of boundary-layer states. The first pair of cases is comprised of a curved-wall zero-pressure-gradient (ZPG) case ZPG-C and a flat-wall ZPG case ZPG-F, the former being achieved through the modification of the domain top pressure profile such that nearly constant mean pressure is induced at the wall. The second pair of cases (PG-C & PG-F) has the same non-zero streamwise pressure gradient along the wall, namely an adverse followed by a favorable pressure gradient. For the flat case PG-F, the pressure distribution applied at the top of the domain is such that the resulting mean wall-pressure distribution matches that of the curved case PG-C.

The primary challenge of the methodology has been the development of a DNS setup which is capable of inducing an arbitrary mean pressure distribution for a given wall geometry, considering that wall pressure cannot be explicitly set for a turbulent/transitional boundary-layer DNS. It has been shown that the appropriate top boundary pressure condition can be obtained for the DNS by using a relatively simple predictor-corrector loop. Such consists of a 2D steady Euler solver tasked with solving for freestream pressure given a wall pressure profile (a relatively ill-posed problem), and a coarse version of the DNS to evaluate how the predicted top pressure performs in terms of inducing a target mean wall pressure. The difference between the 3D coarse simulation and the target wall pressure profile, accounting for real flow effects not taken into account by the 2D solver, is used to correct the input to the 2D predictor for the next iteration. The approach is quickly convergent, relatively straightforward and is more than one order of magnitude less expensive than the DNS itself.

The novelty of the approach is that it enables a clear distinction between the effects of significant streamline curvature and streamwise pressure gradient on the structure and behavior of both laminar and turbulent boundary layers. It makes several cross-comparisons possible, revealing changes to the structure of the boundary layer due to a single variable while controlling for others. For example, the effect of wall curvature with respect to a flat-plate boundary layer can be directly examined, without the complicating influence of non-zero streamwise pressure gradient at the wall. Likewise, for equivalent wall curvatures, the distinct changes due to the presence/absence of streamwise pressure gradient can be investigated. To the knowledge of the authors, the present study design is unique among numerical studies of both laminar and turbulent boundary layers.

The approach has been applied to the case of a subsonic compressible turbulent boundary layer on a concave wall, where it has been verified that the methodology presented can successfully realize DNS setups with well-matched mean wall-pressure distributions. To identify to what extent the effect of streamwise pressure gradient and wall curvature can be isolated in terms of the streamwise evolution of fundamental 1D mean boundary-layer properties such as the wall shear stress τ_w and boundary-layer thickness δ_{99}, a cross-comparison is performed on all four DNS. It has been shown that the effects of streamline curvature and streamwise pressure gradient can be separated remarkably well for the mean flow variables considered, which is a significant finding of the present work made possible by the study's design. However, inspection of wall-normal profiles has confirmed significant interactive influences on the structure of turbulence. The present methodology enables an in-depth investigation of the structure of turbulent boundary layers with streamline curvature in future studies.

Acknowledgements This work was supported by the Deutsche Forschungsgemeinschaft (DFG) in the context of grants RI680/49-1 and WE6803/5-3. The provision of computational resources on HPE Apollo 'Hawk' and NEC SX-Aurora TSUBASA by the Federal High Performance Computing Center Stuttgart (HLRS) under grant GCS-Lamt, project 28956, is gratefully acknowledged.

Funding Open Access funding enabled and organized by Projekt DEAL.

Data Availability The data that support the findings of this study are openly available in a Dataverse repository: https://doi.org/10.18419/darus-4345.

References

1. Arolla, S.K., Durbin, P.A.: LES of spatially developing turbulent boundary layer over a concave surface. J. Turbul. **16**(1), 81–99 (2015). https://doi.org/10.1080/14685248.2014.959126
2. Babucke, A.: Direct numerical simulation of noise-generation mechanisms in the mixing layer of a Jet. Ph.D. thesis, University of Stuttgart (2009)
3. Barlow, R.S., Johnston, J.P.: Structure of a turbulent boundary layer on a concave surface. J. Fluid Mech. **191**, 137–176 (1988). https://doi.org/10.1017/S0022112088001545
4. Boiko, A., Ivanov, A., Kachanov, Y., Mischenko, D.: Steady and unsteady Görtler boundary-layer instability on concave wall. Eur. J. Mech.- B/Fluids **29**(2), 61–83 (2010). https://doi.org/10.1016/j.euromechflu.2009.11.001
5. Bradshaw, P.: Effects of streamline curvature on turbulent flow. Tech. Rep. 169, Advisory Group for Aerospace Research & Development (1973). https://www.sto.nato.int/publications/AGARD/AGARD-AG-169/AGARD-AG-169.pdf
6. Bradshaw, P.: Review-Complex turbulent flows. J. Fluids Eng. **97**(2), 146–154 (1975). https://doi.org/10.1115/1.3447237
7. Brethouwer, G.: Statistics and structure of spanwise rotating turbulent channel flow at moderate Reynolds numbers. J. Fluid Mech. **828**, 424–458 (2017). https://doi.org/10.1017/jfm.2017.526
8. Brethouwer, G.: Turbulent flow in curved channels. J. Fluid Mech. **931**, A21 (2022). https://doi.org/10.1017/jfm.2021.953
9. Clauser, M., Clauser, F.: The effect of curvature on the transition from laminar to turbulent boundary layer. Tech. Rep. 613, National Advisory Committee for Aeronautics (1937). https://ntrs.nasa.gov/api/citations/19930081373/downloads/19930081373.pdf
10. Colonius, T., Lele, S.K., Moin, P.: Boundary conditions for direct computation of aerodynamic sound generation. AIAA J. **31**(9), 1574–1582 (1993). https://doi.org/10.2514/3.11817
11. Ellis, L.B., Joubert, P.N.: Turbulent shear flow in a curved duct. J. Fluid Mech. **62**(1), 65–84 (1974). https://doi.org/10.1017/S0022112074000589

12. Eskinazi, S., Yeh, H.: An investigation on fully developed turbulent flows in a curved channel. J. Aeronaut. Sci. **23**(1), 23–34 (1956). https://doi.org/10.2514/8.3496
13. Floryan, J.M.: Görtler instability of boundary layers over concave and convex walls. Phys. Fluids **29**(8), 2380–2387 (1986). https://doi.org/10.1063/1.865531
14. Gibis, T., Sciacovelli, L., Kloker, M., Wenzel, C.: Heat-transfer effects in compressible turbulent boundary layers - a regime diagram. J. Fluid Mech. **995**, A14 (2024). https://doi.org/10.1017/jfm.2024.622
15. Gibis, T., Wenzel, C., Kloker, M., Rist, U.: Self-similar compressible turbulent boundary layers with pressure gradients. Part 2. Self-similarity analysis of the outer layer. J. Fluid Mech. **880**, 284–325 (2019). https://doi.org/10.1017/jfm.2019.672
16. Gibson, M.: An algebraic stress and heat-flux model for turbulent shear flow with streamline curvature. Int. J. Heat Mass Transf. **21**(12), 1609–1617 (1978). https://doi.org/10.1016/0017-9310(78)90015-7
17. Gillis, J.C., Johnston, J.P.: Turbulent boundary-layer flow and structure on a convex wall and its redevelopment on a flat wall. J. Fluid Mech. **135**, 123–153 (1983). https://doi.org/10.1017/S0022112083002992
18. Gillis, J.C., P., J.J., Kays, W.M., Moffat, R.J.: Turbulent boundary layer on a convex, curved surface. Tech. Rep. HMT-31, Stanford University department of mechanical engineering thermosciences Division (1980). https://ntrs.nasa.gov/api/citations/19810007897/downloads/19810007897.pdf
19. Görtler, H.: Über den Einfluß der Wandkrümmung auf die Entstehung der Turbulenz. ZAMM-J. Appl. Math. Mech./ Zeitschrift für Angewandte Mathematik und Mechanik **20**(3), 138–147 (1940)
20. Görtler, H.: Instabilität laminarer Grenzschichten an konkaven Wänden gegenüber gewissen dreidimensionalen Störungen. ZAMM - J. Appl. Math. Mech./ Zeitschrift für Angewandte Mathematik und Mechanik **21**(4), 250–252 (1941). https://doi.org/10.1002/zamm.19410210408
21. Görtler, H.: On the three-dimensional instability of laminar boundary layers on concave walls. Tech. rep., National Advisory Committee for Aeronautics (1954). https://ntrs.nasa.gov/api/citations/19930093855/downloads/19930093855.pdf
22. Hanjalić, K., Launder, B.E.: A Reynolds stress model of turbulence and its application to thin shear flows. J. Fluid Mech. **52**(4), 609–638 (1972). https://doi.org/10.1017/S002211207200268X
23. Hoffmann, P.H., Muck, K.C., Bradshaw, P.: The effect of concave surface curvature on turbulent boundary layers. J. Fluid Mech. **161**, 371–403 (1985). https://doi.org/10.1017/S0022112085002981
24. Jeans, A.H., Johnston, J.P.: The effects of streamwise concave curvature on turbulent boundary layer structure. Tech. Rep. MD-40, Stanford University (1982). https://apps.dtic.mil/sti/pdfs/ADA122303.pdf
25. Keller, M.A., Kloker, M.J.: Effusion cooling and flow tripping in laminar supersonic boundary-layer flow. AIAA J. **53**(4), 902–919 (2015). https://doi.org/10.2514/1.J053251
26. Keller, M.A., Kloker, M.J.: Direct numerical simulation of foreign-gas film cooling in supersonic boundary-layer flow. AIAA J. **55**(1), 99–111 (2017). https://doi.org/10.2514/1.J055115
27. Kim, W.J., Patel, V.C.: Origin and decay of longitudinal vortices in developing flow in a curved rectangular duct (Data Bank Contribution). J. Fluids Eng. **116**(1), 45–52 (1994). https://doi.org/10.1115/1.2910240
28. Kline, S.J., Cantwell, B.J., Lilley, G.M.: : Complex Turbulent Flows: The 1980-81 AFOSR-HTTM-Stanford Conference on Complex Turbulent Flows: Comparison of Computation and Experiment: Volume I – Objectives, Evaluation of Data, Specifications of Test Cases, Discussion and Position Papers. Tech. Rep. AFOSR-TR-83-1001, Stanford University Department of Mechanical Engineering Thermosciences Division (1982). https://apps.dtic.mil/sti/pdfs/ADA135569.pdf
29. Kline, S.J., Cantwell, B.J., Lilley, G.M.: Complex Turbulent Flows: The 1980-81 AFOSR-HTTM-Stanford Conference on Complex Turbulent Flows: Comparison of Computation and Experiment: Volume II – Taxonomies, Reporters' Summaries, Evaluation and Conclusions. Tech. Rep. AFOSR-TR-83-1002, Stanford University Department of Mechanical Engineering Thermosciences Division (1982). https://apps.dtic.mil/sti/pdfs/ADA135570.pdf
30. Kline, S.J., Cantwell, B.J., Lilley, G.M.: Complex Turbulent Flows: The 1980-81 AFOSR-HTTM-Stanford Conference on Complex Turbulent Flows: Comparison of Computation and Experiment: Volume III – Comparison of Computation with Experiment and Computors Summary Reports. Tech. Rep. AFOSR-TR-83-1003, Stanford University Department of Mechanical Engineering Thermosciences Division (1982). https://apps.dtic.mil/sti/pdfs/ADA136034.pdf
31. Kloker, M.J.: A robust high-resolution split-type compact FD scheme for spatial direct numerical simulation of boundary-layer transition. Flow, Turbul. Combust. **59**, 353–377 (1997). https://doi.org/10.1023/A:1001122829539
32. Launder, B.E., Priddin, C.H., Sharma, B.I.: The calculation of turbulent boundary layers on spinning and curved surfaces. J. Fluids Eng. **99**(1), 231–239 (1977). https://doi.org/10.1115/1.3448528
33. Launder, B.E., Reece, G.J., Rodi, W.: Progress in the development of a Reynolds-stress turbulence closure. J. Fluid Mech. **68**(3), 537–566 (1975). https://doi.org/10.1017/S0022112075001814
34. Linn, J., Kloker, M.J.: Numerical investigations of film cooling. In: A. Gülhan (ed.) RESPACE – Key Technologies for Reusable Space Systems, pp. 151–169. Springer Berlin Heidelberg, Berlin, Heidelberg (2008). https://doi.org/10.1007/978-3-540-77819-6_9
35. Linn, J., Kloker, M.J.: Effects of wall-temperature conditions on effusion cooling in a supersonic boundary layer. AIAA J. **49**(2), 299–307 (2011). https://doi.org/10.2514/1.J050383
36. Lund, T.S., Moin, P.: Large-eddy simulation of a concave wall boundary layer. Int. J. heat fluid flow **17**(3), 290–295 (1996). https://doi.org/10.1016/0142-727X(96)00039-2
37. Meroney, R.N., Bradshaw, P.: Turbulent boundary-layer growth over a longitudinally curved surface. AIAA J. **13**(11), 1448–1453 (1975). https://doi.org/10.2514/3.7014
38. Monson, D.J., Seegmiller, H.L., McConnaughey, P.K.: Comparison of LDV Measurements and Navier-Stokes Solutions in a Two-Dimensional 180-Degree Turn-Around Duct. In: 27th Aerospace Sciences Meeting (1989). https://doi.org/10.2514/6.1989-275
39. Monson, D.J., Seegmiller, H.L., McConnaughey, P.K., Chen, Y.S.: Comparison of experiment with calculations using curvature-corrected zero and two equation turbulence models for a two-dimensional U-duct. In: 21st Fluid Dynamics, Plasma Dynamics and Lasers Conference (1990). https://doi.org/10.2514/6.1990-1484
40. Moser, R.D., Moin, P.: The effects of curvature in wall-bounded turbulent flows. J. Fluid Mech. **175**, 479–510 (1987). https://doi.org/10.1017/S0022112087000491

41. Muck, K.C., Hoffmann, P.H., Bradshaw, P.: The effect of convex surface curvature on turbulent boundary layers. J. Fluid Mech. **161**, 347–369 (1985). https://doi.org/10.1017/S002211208500297X
42. Nagata, M., Kasagi, N.: Spatio-temporal evolution of coherent vortices in wall turbulence with streamwise curvature. J. Turbul. **5**(1), 017 (2004). https://doi.org/10.1088/1468-5248/5/1/017
43. Pargal, S., Wu, H., Yuan, J., Moreau, S.: Adverse-pressure-gradient turbulent boundary layer on convex wall. Phys. Fluids **10**(1063/5), 0083919 (2022)
44. Patel, V.C.: The effects of curvature on the turbulent boundary layer. Tech. Rep. 3599, Ministry of Technology (1969). https://reports.aerade.cranfield.ac.uk/handle/1826.2/2867
45. Prandtl, L.: Einfluß stabilisierender Kräfte auf die Turbulenz. In: Tollmien et al. [61], pp. 778–785. https://doi.org/10.1007/978-3-662-11836-8_62
46. Prandtl, L.: Effect of stabilizing forces on turbulence. Tech. Rep. 625, National Advisory Committee for Aeronautics (1931). https://ntrs.nasa.gov/citations/19930094791
47. Ramaprian, B., Shivaprasad, B.: The structure of turbulent boundary layers along mildly curved surfaces. J. Fluid Mech. **85**(2), 273–303 (1978). https://doi.org/10.1017/S0022112078000646
48. Rayleigh, L.: On the dynamics of revolving fluids. Proce. Royal Soc. London **93**(648), 148–154 (1917). https://doi.org/10.1098/rspa.1917.0010
49. Rodi, W., Scheuerer, G.: Calculation of curved shear layers with two-equation turbulence models. Phys. Fluids **26**(6), 1422–1436 (1983). https://doi.org/10.1063/1.864312
50. Schwarz, A.C., Plesniak, M.W.: The influence of interacting strain rates on turbulence in convex boundary layers. Phys. Fluids **8**(11), 3163–3171 (1996). https://doi.org/10.1063/1.869089
51. Shizawa, T., Honami, S.: Experiment on turbulent boundary layers over a concave surface : effects of introduction of curvature. In: Fourth Symposium on Turbulent Shear Flows, p. 6.38. University of Karlsruhe, Karlsruhe, West Germany (1983). https://apps.dtic.mil/sti/pdfs/ADA135034.pdf
52. Shur, M.L., Strelets, M.K., Travin, A.K., Spalart, P.R.: Turbulence modeling in rotating and curved channels: assessing the spalart-shur correction. AIAA J. **38**(5), 784–792 (2000). https://doi.org/10.2514/2.1058
53. Smits, A.J., Young, S., Bradshaw, P.: The effect of short regions of high surface curvature on turbulent boundary layers. J. Fluid Mech. **94**(2), 209–242 (1979). https://doi.org/10.1017/S0022112079001002
54. So, R.M.C., Mellor, G.L.: Experiment on convex curvature effects in turbulent boundary layers. J. Fluid Mech. **60**(1), 43–62 (1973). https://doi.org/10.1017/S0022112073000030
55. So, R.M.C., Mellor, G.L.: Experiment on turbulent boundary layers on a concave wall. Aeronaut. Q. **26**(1), 25–40 (1975). https://doi.org/10.1017/S0001925900007174
56. Souza, LFd., Mendonça, MTd., Medeiros, M.AFd., Kloker, M.: Seeding of Görtler vortices through a suction and blowing strip. J. Braz. Soc. Mech. Sci. Eng. **26**, 269–279 (2004). https://doi.org/10.1590/S1678-58782004000300003
57. Spalart, P.R., Allmaras, S.R.: A one-equation turbulence model for aerodynamic flows. La Recherche Aérospatiale p. 5–21 (1994)
58. Spalart, P.R., Strelets, M.K.: Mechanisms of transition and heat transfer in a separation bubble. J. Fluid Mech. **403**, 329–349 (2000). https://doi.org/10.1017/S0022112099007077
59. Tani, I.: Production of longitudinal vortices in the boundary layer along a concave wall. J. Geophys. Res. **67**(8), 3075–3080 (1962). https://doi.org/10.1029/JZ067i008p03075
60. Taylor, G.I.: Stability of a viscous liquid contained between two rotating cylinders. Philos. Trans. Royal Soc. London Ser. A, Contain. Papers Math. Phys. Character **223**, 289–343 (1923). https://doi.org/10.1098/rsta.1923.0008
61. Tollmien, W., Schlichting, H., Görtler, H., Riegels, F.W.: Ludwig Prandtl Gesammelte Abhandlungen: zur angewandten Mechanik, Hydro- und Aerodynamik. Springer, Berlin (1961). https://doi.org/10.1007/978-3-662-11836-8
62. Visbal, M.R., Gaitonde, D.V.: On the use of higher-order finite-difference schemes on curvilinear and deforming meshes. J. Comput. Phys. **181**(1), 155–185 (2002). https://doi.org/10.1006/jcph.2002.7117
63. Wattendorf, F.L.: A study of the effect of curvature on fully developed turbulent flow. Proc. Royal Soc. London Ser. A-Math. Phys. Sci. **148**, 565–598 (1935). https://doi.org/10.1098/rspa.1935.0034
64. Wenzel, C.: DNS of compressible turbulent boundary layers: pressure-gradient influence and self-similarity. Ph.D. thesis, University of Stuttgart (2019)
65. Wenzel, C., Gibis, T., Kloker, M., Rist, U.: Self-similar compressible turbulent boundary layers with pressure gradients. Part 1. Direct numerical simulation and assessment of Morkovin's hypothesis. J. Fluid Mech. **880**, 239–283 (2019). https://doi.org/10.1017/jfm.2019.670
66. Wenzel, C., Selent, B., Kloker, M., Rist, U.: DNS of compressible turbulent boundary layers and assessment of data/scaling-law quality. J. Fluid Mech. **842**, 428–468 (2018). https://doi.org/10.1017/jfm.2018.179
67. Wilcken, H.: Turbulente Grenzschichten an gewölbten Flächen. Ingenieur-Archiv **1**, 357–376 (1930). https://doi.org/10.1007/BF02095927
68. Yang, X., Tucker, P.G.: Assessment of turbulence model performance: large streamline curvature and integral length scales. Comput. Fluids **126**, 91–101 (2016). https://doi.org/10.1016/j.compfluid.2015.11.010
69. You, J., Buchta, D.A., Zaki, T.A.: Concave-wall turbulent boundary layers without and with free-stream turbulence. J. Fluid Mech. **915**, A4 (2021). https://doi.org/10.1017/jfm.2021.12